Available online at www.sciencedirect.com
ScienceDirect
Journal of Sound and Vibration 315 (2008) 911–926
JOURNAL OF SOUND AND VIBRATION
www.elsevier.com/locate/jsvi

Nonlinear modeling of composite plates with piezoceramic layers using finite element analysis

Ziya K. Kusculuoglu, Thomas J. Royston*

Department of Mechanical Engineering, University of Illinois at Chicago, 2039 Engineering Research Facility, 842 West Taylor Street, Mail Code 251, Chicago, IL 60607-7022, USA

Accepted 7 June 2007
The peer review of this article was organised by the Guest Editor
Available online 11 April 2008

Abstract

A finite element formulation for the vibration of piezoceramic laminated plates that takes hysteretic behavior into account is presented. Structural deformations of the layers are modeled using Mindlin plate theory where electro-mechanical coupling equations are formulated based on the same theory. Electro-mechanical coupling terms model orthotropic piezoelectric properties ($g_{31} \neq g_{32}$), in addition to an orthotropic formulation for the mechanical properties of each plate layer. Lateral and transversal displacement fields are modeled with 8-node serendipity quadratic elements. Hysteretic behavior within the dielectric domain is implemented and simulated via the finite element method using an Ishlinskii model. Experimental hysteresis characterization for a single piezo layer and simulation results are presented. A coupled composite plate model is also tested under different loading conditions experimentally and numerically.

1. Introduction

Applications of smart material systems with piezoelectric actuators have been increasing for the last quarter century due to their fast response time, structural stiffness and suitability for control. The dynamics of piezoelectric devices offer a competitive edge over other technologies providing high precision with high resolution, even to the microscale.

However, one disadvantage of piezoceramic devices is their inherent nonlinear behavior even at low field levels due to hysteresis in the dielectric domain. Hysteretic ferroelectric behavior makes position control and tracking applications challenging as the actuator's response is dependent on past extrema.

Ferromagnetic and magnetostrictive hysteresis has been investigated by many authors. Mayergoyz, Friedman and Adly [1–4] have developed a hysteresis model based on the classical Preisach model, with a

*Corresponding author. Tel.: +1 312 413 7951.
E-mail address: troyston@uic.edu (T.J. Royston).

0022-460X/$ - see front matter © 2008 Elsevier Ltd. All rights reserved.
doi:10.1016/j.jsv.2007.06.081

detailed system identification scheme for the Preisach model given by Mayergoyz [5]. Delince and Nicolet [6] investigated the hysteresis effect on coupled finite element problems based on a lumped element approach where the hysteretic behavior of the magnetic material was modeled by computing the flux density via a linear combination of the Everett function. Various other researchers have investigated modeling the ferromagnetic hysteresis problem using the finite element method [7–10].

With regard to piezoceramic hysteresis, in 1995 Ge and Jouaneh [11] discussed the adaptation of the Preisach model to piezoceramic actuators for a control application problem. Jung and Kim [12] have introduced 3 different hysteresis models for a feedforward control application where the models were based on the saturated state of the PZT. In 1998 Coutte et al. [13] proposed an electrostrictive finite element model for nonlinear static and time domain analysis. In their model the piezoelectric strain constant and the dielectric impermittivity constants are defined as nonlinear operators and they are implemented into the classical coupled field system equation. Simkovics et al. [14,15] have developed a finite element formulation for the hysteretic piezoelectric effect using virtual displacements of the system. In the formulation the elastic, piezoelectric and dielectric constant tensors are dependent on the applied electric field, which introduces nonlinearity to the formulation; also the strain tensor is expanded to second-order Lagrangean strains for the geometric nonlinearities. Song and Li [16] have developed a hybrid hysteresis model using the classical Preisach model and neural networks, but their work was not extended to finite element applications as they focused on online model identification. Goldfarb and Celanovic [17] have used a Maxwell resistive-capacitor model, a specific type of Preisach model, for the simulation of the rate-independent hysteresis in stack actuators and the electro-mechanical coupling; however, their work was an analytic formulation. In 2001 Krejci and Kuhnen [18] proposed an operator-based hysteresis and creep modeling and its inverse operator for control purposes that deals with both phenomena at the same time. Kamlah and Bohle [19] developed a finite element method for investigation of the ferroelectric hysteresis behavior where they solved the electric potential history and then used this to conduct the electro-mechanical analysis; the study was extended to a stack actuator simulation. More recently researchers [20–24] have proposed improved Preisach-type hysteresis models and their implementation to neural networks. Smith et al. [25,26] modeled piezoelectric hysteresis using Gibbs and Helmholtz energy relations and Zirka et al. [27] proposed a history-dependent non-Preisach model using first-order reversal curves and a congruency-based model. Royston et al. [28–30] adapted the Ishlinskii hysteresis model (a specific type of Preisach model analogous to the Maxwell resistive-capacitor model) to piezoceramic transducers for vibration control.

In this paper, the authors introduce a nonlinear operator to the coupled system equations to predict the hysteretic piezoelectric behavior when using the multilayered plate finite element formulation. The study includes the experimental identification of the Ishlinskii hysteresis operators and the verification of the finite element results by experiments for different excitation cases.

2. Modeling and theory

2.1. Constitutive linear model

Conventional Mindlin plate theory is used as the constitutive relationships for the plate element with piezoelectric properties. It is derived to have 8-node serendipity quadratic shape functions and have 5 degrees of freedom for each node $\{u,v,\psi_x,\psi_y,w\}$ as illustrated in Fig. 1. Here, u and v are the lateral mid-plane displacement in x and y directions, ψ_x and ψ_y are the independent rotations of the normal in x–z and y–z planes, and w is the transverse displacement of the mid-plane. Accordingly, the displacement field equations can be written as

$$\begin{aligned} u_{11} &= u(x,y,t) - z\psi_x(x,y,t), \\ u_{22} &= v(x,y,t) - z\psi_y(x,y,t), \\ u_{33} &= w(x,y,t). \end{aligned} \tag{1}$$

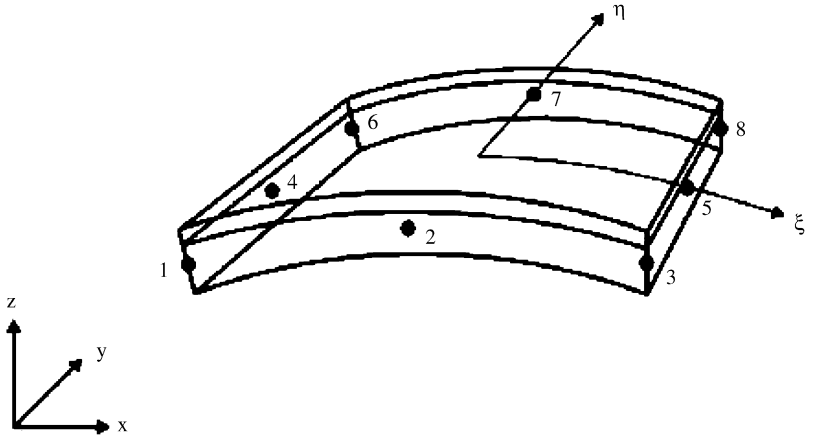

Fig. 1. Coordinate systems for 8-node quadratic serendipity element for 2 layers.

It is assumed that each layer undergoes the same displacement as the mid-plane of the laminated plate. According to this, the strain and stress equations should be written as

$$\begin{Bmatrix} \varepsilon_{11} \\ \varepsilon_{22} \\ 2\varepsilon_{12} \\ 2\varepsilon_{13} \\ 2\varepsilon_{23} \end{Bmatrix} = \begin{Bmatrix} \dfrac{\partial u}{\partial x} - z\dfrac{\partial \psi_x}{\partial x} \\ \dfrac{\partial v}{\partial y} - z\dfrac{\partial \psi_y}{\partial y} \\ \dfrac{\partial u}{\partial y} + \dfrac{\partial v}{\partial x} - z\left(\dfrac{\partial \psi_x}{\partial y} + \dfrac{\partial \psi_y}{\partial x}\right) \\ -\psi_x + \dfrac{\partial w}{\partial x} \\ -\psi_x + \dfrac{\partial w}{\partial y} \end{Bmatrix}, \tag{2}$$

$$\begin{Bmatrix} \sigma_{11}^k \\ \sigma_{22}^k \\ \sigma_{12}^k \\ \sigma_{13}^k \\ \sigma_{23}^k \end{Bmatrix} = \begin{bmatrix} c_{11}^k & c_{12}^k & 0 & 0 & 0 \\ c_{21}^k & c_{22}^k & 0 & 0 & 0 \\ 0 & 0 & c_{33}^k & 0 & 0 \\ 0 & 0 & 0 & c_{44}^k & 0 \\ 0 & 0 & 0 & 0 & c_{55}^k \end{bmatrix} \begin{Bmatrix} \varepsilon_{11} \\ \varepsilon_{22} \\ 2\varepsilon_{12} \\ 2\varepsilon_{13} \\ 2\varepsilon_{23} \end{Bmatrix}. \tag{3}$$

In Eq. (3), σ^k and c^k represent the mechanical stress and the elastic constant for the kth layer, respectively. If the layer is a piezoactuator/sensor, then the first two stress terms for the piezo (pz) layer in the stress equation would be written as

$$\begin{Bmatrix} \sigma_{11}^{pz} \\ \sigma_{22}^{pz} \end{Bmatrix} = \begin{bmatrix} \dfrac{E_1^{pz}}{1-\upsilon_{12}^{pz}\upsilon_{21}^{pz}} & \dfrac{E_1^{pz}\upsilon_{21}^{pz}}{1-\upsilon_{12}^{pz}\upsilon_{21}^{pz}} \\ \dfrac{E_2^{pz}\upsilon_{12}^{pz}}{1-\upsilon_{12}^{pz}\upsilon_{21}^{pz}} & \dfrac{E_2^{pz}}{1-\upsilon_{12}^{pz}\upsilon_{21}^{pz}} \end{bmatrix} \begin{Bmatrix} \varepsilon_{11}^{pz} \\ \varepsilon_{22}^{pz} \end{Bmatrix} - \begin{bmatrix} h_{31} \\ h_{32} \end{bmatrix} \{D_3\}. \tag{4}$$

Here, two-dimensional piezoceramic equations are given under the following assumptions: $\sigma_{33} = D_1 = D_2 = E_1 = E_2 = 0$, where D_3 is the electric displacement occurring in the 3 directions and h_{31} and h_{32} are the piezoelectric constants for 31 and 32 directions, E_1^{pz} and E_2^{pz} are Young's Moduli of the piezo layer in the 1 and 2 directions, and υ_{12}^{pz} and υ_{21}^{pz} are the Poisson's ratios. The electro-mechanical coupling is defined in 31 and 32 directions and orthotropic assumptions are made. For the linear case, coupling equations are completed by

defining the electric field E in terms of electric displacement D_3 and mechanical stress σ

$$[E] = \begin{bmatrix} -g_{31} & -g_{32} & \beta_{33}^{\sigma} \end{bmatrix} \begin{bmatrix} \sigma_{11}^{pz} \\ \sigma_{22}^{pz} \\ D_3 \end{bmatrix}. \tag{5}$$

Here, g_{31} and g_{32} are the piezoelectric constants and β_{33}^{σ} is the dielectric impermeability constant for the piezo layer.

2.2. Nonlinear Ishlinskii hysteresis operator

Hysteresis in piezoelectric ceramics is a well known, primarily though not entirely rate-independent phenomenon that occurs even with low electric fields or low mechanical stress conditions that cannot be modeled using reversible relationships between the electric field (E) and the electric displacement (D) or the stress (σ) given in Eq. (5). In the literature [31] it has been reported that the relationship between the electric displacement (D) and mechanical strain (S) under zero stress (σ) is reversible; but, the applied electric field (E) vs. (S) under zero stress is not reversible. This relationship is expressed as follows [28–30]:

$$[E] = \begin{bmatrix} -g_{31} & -g_{32} \end{bmatrix} \begin{bmatrix} \sigma_{11}^{pz} \\ \sigma_{22}^{pz} \end{bmatrix} + \mathrm{IM}\{\beta_{33}^{\sigma} D_3\}. \tag{6}$$

Here, $\mathrm{IM}\{\beta_{33}^{\sigma} D_3\}$ is a nonlinear operator that symbolizes the Ishlinskii hysteresis model. Eq. (6) ties the single input $\beta_{33}^{\sigma} D_3$ to a single output quantity $\{\beta_{33}^{\sigma} D_3\}$ where, if the mechanical stress that the piezo structure is subjected to is zero, then the electric field (E) is simply equal to $\{\beta_{33}^{\sigma} D_3\}$. Again, if the mechanical stress terms are zero, the inverse relationship can be written as $D = \{E\}^{-1}/\beta_{33}^{\sigma}$, where the electric field (E) is the input and the electric displacement is the output.

The Ishlinskii hysteresis operator and its inverse are special cases of the classical Preisach model which means that *wiping out* and *congruency* conditions are satisfied [32]. A classical Preisach model defines a mathematical mapping between the input $u(t)$ and the output $f(t)$ for a rate-independent irreversible thermodynamic process

$$f(t) = \iint_{\alpha \geqslant \beta} \mu(\alpha, \beta) \gamma_{\alpha\beta}[u(t)] \, \mathrm{d}\alpha \, \mathrm{d}\beta. \tag{7}$$

Here, the input–output relationship given in Eq. (7) is defined by the relay operator $\gamma_{\alpha\beta}$ and the weighting function $\mu(\alpha,\beta)$ where α and β symbolize the extrema values of the input function $u(t)$. The Ishlinskii hysteresis operator can be described in analogy as a group of sliding blocks with Coulomb friction (Fig. 2).

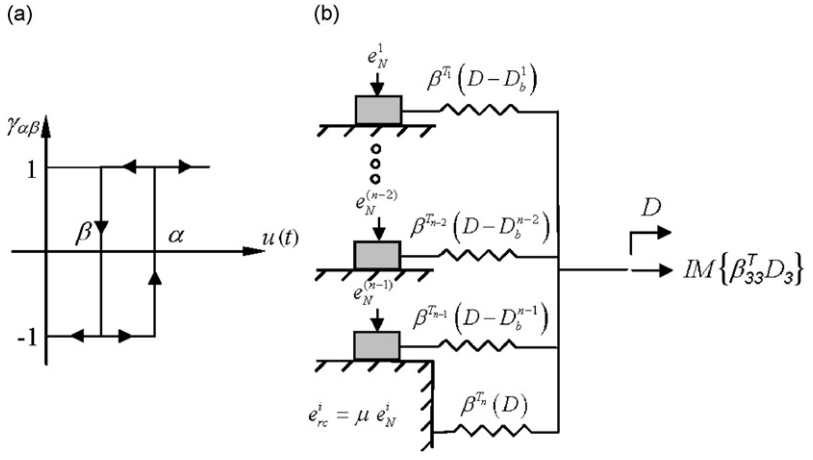

Fig. 2. (a) Preisach relay operator and (b) mechanical analogy of the Ishlinskii hysteresis model.

With this analogy, the dielectric impermeability (β^{σ}) under uniform stress can be considered as a spring coefficient, μ as the friction coefficient, e_N as the normal force acting on the element, and e_{rc} as the friction force acting on the massless block. As illustrated in Fig. 2b, when the displacement input D is given to the system the resultant accumulative force becomes the output $\{\beta^{\sigma}_{33}D_3\}$.

The last spring element shown in Fig. 2 is connected to a wall with no sliding block in order to simulate the saturation at the maximum and the minimum input values. This model can be described by

$$\mathrm{IM}\{\beta^{\sigma}D\} = \sum_{i=1}^{n} E^i_{rc}, \quad \text{where } i = 1, 2, \ldots, n, \tag{8}$$

$$\text{if } |\beta^{\sigma i}(D - D^i_b)| < e^i_{rc} \quad \text{then} \quad E^i_{rc} = \beta^{\sigma i}(D - D^i_b)$$

$$\text{else} \quad E^i_{rc} = e^i_{rc}\,\mathrm{sign}[\dot{D}] \text{ and } D^i_b \text{ such that } |\beta^{\sigma}_i(D - D^i_b)| = e^i_{rc}.$$

The input–output relationship given in Eq. (8) can be graphically represented as shown in Fig. 3 for the case when $n = 2$.

This system can be described using the Preisach model and the generalized weighting function for n blocks is

$$\mu(\alpha, \beta) = \frac{1}{2}\left\{\sum_{i=1}^{n}(\beta^{\sigma i})\delta[\alpha - \beta] - \sum_{i=1}^{n-1}(\beta^{\sigma i}\delta[\alpha - \beta - w_i])\right\}. \tag{9}$$

Here, δ is the Dirac delta function and $w_i = 2e^i_{rc}/\beta^{\sigma i}$. By using Eq. (7), and choosing the electric field (E) to be the output, the following equation can be written:

$$E(t) = \int_{\alpha_1}^{\alpha_2} \frac{1}{2}\left\{\sum_{i=1}^{n}(\beta^{\sigma i})\gamma_{\alpha,\alpha} - \sum_{i=1}^{n-1}(\beta^{\sigma i}\gamma_{\alpha,\alpha-w_i})\right\} D_3(t)\,\mathrm{d}\alpha. \tag{10}$$

Here the defined function represents the Ishlinskii model that satisfies 4 distinct properties:

(1) the weighting function $\mu(\alpha,\beta)$ consists of countable number of lines parallel to the $\alpha = \beta$ line,
(2) the number of lines corresponds to the number of Ishlinskii sliding blocks,
(3) each line has a constant value along its length, and
(4) this constant value is dependent on the sliding element properties.

Model identification of the Ishlinskii model assumes symmetric hysteresis loops where the absolute values of the extrema and minima are same $|\alpha_0| = |\beta_0|$ as illustrated in Fig. 4. Just like the classical Preisach model, identification is achieved by determining the first-order reversal curves, which can be represented by the Everett function.

Using this function the elastic coefficients (β^{σ}) and the sliding constants (e_{rc}) shown in Fig. 2b are obtained. Further details of the model identification scheme can be found in the literature [28–30].

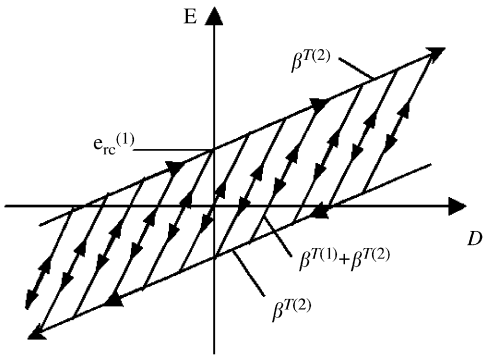

Fig. 3. Ishlinskii model with 2 springs and a sliding block.

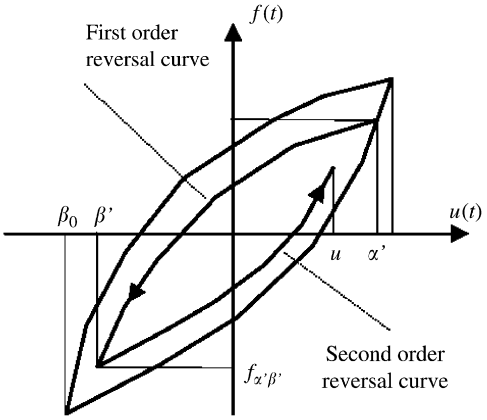

Fig. 4. First-order reversal curves for the input–output relationship.

3. Finite element model

In this section the potential and kinetic energy equations are derived where mechanical and electro-mechanical potential energy equations are decoupled from each other. The formulation is derived so that energy terms of each layer are evaluated based on a Mindlin plate theory. In this work unlike the previous work of the authors [33], where a linear formulation was presented, the displacement field constraining equations are not enforced and it is assumed that each layer undergoes the same type of deformation.

3.1. Mechanical potential energy terms

The mechanical potential energy for the non-piezo layers is calculated by defining the strain energy U^k for the infinitesimal deformation term for the kth layer of the composite plate as

$$U^k = \frac{1}{2}\int_{\Omega^e}\left[\int_{-h_k^e/2}^{h_k^e/2}\{\varepsilon_{11} \quad \varepsilon_{22} \quad 2\varepsilon_{12} \quad 2\varepsilon_{13} \quad 2\varepsilon_{23}\}\{\sigma_{11}^k \quad \sigma_{22}^k \quad \sigma_{12}^k \quad \sigma_{13}^k \quad \sigma_{23}^k\}^{\mathrm{T}}\,\mathrm{d}z\right]\mathrm{d}x\,\mathrm{d}y, \tag{11}$$

where Ω^e is the elemental domain, h_k^e is the thickness and σ_{ij}^n is the stress term of the kth layer. Stress equations are defined in Eq. (3) which is written in short form as

$$\{\boldsymbol{\sigma}^k\} = [\mathbf{C}^k]\{\boldsymbol{\varepsilon}\}. \tag{12}$$

3.2. Electro-mechanical potential energy terms

In the experimental application presented in this study the monolithic piezoceramic (PZT) is the top layer of the composite plate. (For different applications the piezoceramic can be other layers.) For this reason the top indices for the equations are named as "pz" rather than the layer number (as in, e.g., Eq. (4)). Mechanical stress and potential energy equations for the piezo layer independent of the electric displacement were given in Eqs. (11) and (12). Coupling terms of the stress with the electrical displacement for the energy expression can be written as

$$U_{p'} = \frac{1}{2}\int_{\Omega^e}\left[\int_{-h_{pz}^e/2}^{h_{pz}^e/2}\begin{bmatrix}-h_{31} & -h_{32}\end{bmatrix}\begin{Bmatrix}\varepsilon_{11}\\ \varepsilon_{22}\end{Bmatrix}\{D_3\}\,\mathrm{d}z\right]\mathrm{d}x\,\mathrm{d}y. \tag{13}$$

The potential energy of the dielectric effect of the piezo layer can be expressed as

$$U_{pe} = \frac{1}{2}\int_{V_{pz}^e}(E_3\{D_3\})\,\mathrm{d}V, \tag{14}$$

where $V_{pz}^{e} = \Omega^{e}(-\frac{1}{2}h^{pz}, \frac{1}{2}h^{pz})$, so Eq. (14) can be explicitly written as

$$U_{pe} = \frac{1}{2}\int_{\Omega^e}\left[\int_{-h_{pz}^{e}/2}^{h_{pz}^{e}/2}\left(\mathrm{IM}\{\beta_{33}^{\sigma}D_3\}\{D_3\} + \begin{bmatrix} -g_{31} & -g_{32}\end{bmatrix}\begin{Bmatrix}\sigma_{11}^{pz}\\ \sigma_{11}^{pz}\end{Bmatrix}\{D_3\}\right)\mathrm{d}z\right]\mathrm{d}x\,\mathrm{d}y. \tag{15}$$

3.3. Kinetic energy terms

The kinetic energy equations will be the same for each layer. Accordingly, the element kinetic energy of the nth layer can be written as

$$T^{k} = \frac{1}{2}\rho^{k}\int_{\Omega^e}\left[\int_{-h_k^e/2}^{h_k^e/2}(\{\dot{\underline{\mathbf{u}}}\}^{\mathrm{T}}\{\dot{\underline{\mathbf{u}}}\})\,\mathrm{d}z\right]\mathrm{d}x\,\mathrm{d}y. \tag{16}$$

In Eq. (16), ρ^k is the density of the kth layer and $\{\dot{\underline{\mathbf{u}}}\}$ is the time derivative of the vector that stores the displacement field terms defined by the independent generalized coordinates, which are obtained by using the constraining equation given in Eq. (1).

3.4. Element matrices and equations of motion

Generalized nodal coordinates stored in the $\{\mathbf{q}\}$ vector can be approximated by using shape functions ϕ_j over the domain Ω^e. Here kk is the number of nodes per element and $\mathbf{q}_i$ is the vector that stores the independent variables for the ith node

$$\{\mathbf{q}\} = \left\{\sum_{j=1}^{kk}\phi_j(u^1)_j \quad \sum_{j=1}^{kk}\phi_j(v^1)_j \quad \sum_{j=1}^{kk}\phi_j(\psi_x^1)_j \quad \sum_{j=1}^{kk}\phi_j(\psi_y^1)_j \quad \cdots \quad \sum_{j=1}^{kk}\phi_j(w)_j\right\}^{\mathrm{T}}. \tag{17a}$$

Eq. (17a) can be simplified as below where $\{\mathbf{\Delta}\}$ is the elemental nodal coordinate vector:

$$\{\mathbf{q}\} = [\mathbf{\Psi}]\{\mathbf{\Delta}\}. \tag{17b}$$

By using Eqs. (17b) and (2), virtual displacements and virtual strains can be written as

$$\{\delta\mathbf{q}\} = [\mathbf{\Psi}]\{\delta\mathbf{\Delta}\}, \tag{18}$$

$$\{\delta\boldsymbol{\varepsilon}\} = [\mathbf{H}][\mathbf{T}][\mathbf{\Psi}]\{\delta\mathbf{\Delta}\}, \tag{19}$$

respectively. Here, $[\mathbf{T}]$ represents the matrix for the differential operators and $[\mathbf{H}]$ is the matrix that stores the truncated constants matrix from Eq. (2). Similarly, virtual displacement field equations can be represented in terms of the elemental nodal coordinate vector using Eq. (2) as

$$\{\delta\,\underline{\mathbf{u}}\} = [\mathbf{S}][\mathbf{\Psi}]\{\delta\mathbf{\Delta}\}. \tag{20}$$

In Eq. (20), $[\mathbf{S}]$ is the matrix where all of the displacement field relations are truncated. Using the virtual displacements defined in Eq. (18), the virtual work done by the external forces can be defined as

$$\delta W_d = \int_{\Omega^e}\mathbf{f}\,\delta\mathbf{q}\,\mathrm{d}x\,\mathrm{d}y. \tag{21}$$

According to the Hamilton's principle one can write,

$$\int_{t_1}^{t_2}\left[\sum_{k=1}^{n}(\delta T^k - \delta E^k) - \delta E_p - \delta E_{pe} - \delta E_{p'} + \delta W_d\right]\mathrm{d}t = 0. \tag{22}$$

Element mass and stiffness matrices for the system can be written as shown below by using Eqs. (11)–(22):

$$\mathbf{M}^{e} = \int_{\Omega^e}\left[\int_{-h_k^e/2}^{h_k^e/2}\sum_{k=1}^{n}(\rho^k([\mathbf{\Psi}]^{\mathrm{T}}[\mathbf{S}]^{\mathrm{T}}[\mathbf{S}][\mathbf{\Psi}]))\,\mathrm{d}z\right]\mathrm{d}x\,\mathrm{d}y, \tag{23}$$

$$\mathbf{K}_{qq}^{e}=\int_{\Omega^e}\left[\int_{-h_k^e/2}^{h_k^e/2}\sum_{k=1}^{n}(([\mathbf{\Psi}]^{\mathrm{T}}[\mathbf{T}]^{\mathrm{T}}[\mathbf{H}]^{\mathrm{T}}[\mathbf{C}^{k}][\mathbf{H}][\mathbf{T}][\mathbf{\Psi}]))\,\mathrm{d}z\right]\mathrm{d}x\,\mathrm{d}y. \tag{24}$$

By using Eqs. (13), (17) and (19) the electro-mechanical coupling vector $\mathbf{K}_{qQ}^{e}$ that combines the electrical and mechanical domains can be written as

$$\mathbf{K}_{qQ}^{e}=\frac{1}{2A^e}\int_{\Omega^e}\left[\int_{-h_{pz}^e/2}^{h_{pz}^e/2}\left(\left(\begin{bmatrix}-h_{31}\\-h_{32}\end{bmatrix}^{\mathrm{T}}[\mathbf{H}][\mathbf{T}][\mathbf{\Psi}]+\begin{bmatrix}-g_{31}\\-g_{32}\end{bmatrix}^{\mathrm{T}}[\mathbf{C}^{pz}][\mathbf{H}][\mathbf{T}][\mathbf{\Psi}]\right)\right)\mathrm{d}z\right]\mathrm{d}x\,\mathrm{d}y. \tag{25}$$

Here, A^e is the total area of the piezo layer (the area of the element) in the x–y plane. The last term obtained from Eq. (22) would be the inverse capacitance, shown as K_{QQ}, depending on whether it is for the sensor or the actuator layer, and is equal to:

$$K_{QQ}=h_{pz}\left(\frac{1}{A^e}(g_{31}h_{31}+g_{312}h_{32})+\frac{\mathrm{IM}\{\beta_{33}^{\sigma}D_3\}}{Q}\right). \tag{26}$$

Defining the mass and stiffness matrices along with the coupling term and the inverse capacitance, the equation of motion for a system with a single patch can be constructed:

$$\begin{bmatrix}\mathbf{M}&0\\0&L\end{bmatrix}\begin{Bmatrix}\ddot{\mathbf{q}}\\\ddot{Q}\end{Bmatrix}+\begin{bmatrix}\mathbf{C}&0\\0&R\end{bmatrix}\begin{Bmatrix}\dot{\mathbf{q}}\\\dot{Q}\end{Bmatrix}+\begin{bmatrix}\mathbf{K}_{qq}&\mathbf{K}_{qQ}\\\mathbf{K}_{Qq}&\{K_{QQ}\}\end{bmatrix}\begin{Bmatrix}\mathbf{q}\\Q\end{Bmatrix}=\begin{bmatrix}\mathbf{F}\\V\end{bmatrix}, \tag{27}$$

where $\mathbf{M}$, $\mathbf{C}$, $\mathbf{K}_{\mathrm{qq}}$ are the assembled mass, damping, and stiffness matrices, respectively, and, $[\mathbf{K}_{qQ}]$ is the assembled electro-mechanical coupling vector for the piezo layer. $[\mathbf{K}_{Qq}]$ is the transpose of $[\mathbf{K}_{qQ}]$. L is the inductance and R is the resistance that can be shunted across the piezo layer and, $\mathbf{F}$ and V are, respectively, the external force vector and external voltage applied to the PZT wafer.

Defining the equation of motion for the system, one can expand the matrix notation into a system of equations as

$$\begin{gathered}\mathbf{M}\ddot{\mathbf{q}}+\mathbf{C}\dot{\mathbf{q}}+\mathbf{K}_{qq}\mathbf{q}+\mathbf{K}_{qQ}Q=\mathbf{F},\\ L\ddot{Q}+R\dot{Q}+\mathbf{K}_{Qq}\mathbf{q}+\frac{h_{pz}}{A^e}(g_{31}h_{31}+g_{312}h_{32})Q+h_{pz}IM\left\{\beta_{33}^{\sigma}\frac{Q}{A^e}\right\}]=V.\end{gathered} \tag{28}$$

At this point the system equations can be converted to state space form, where the state space variables are selected as shown in Eq. (29a). Here, $\mathbf{q}$ is the generalized coordinate vector and Q is the electric charge.

$$\{\boldsymbol{\chi}\}=\begin{Bmatrix}\chi_1&\chi_3&\chi_2&\chi_4\end{Bmatrix}^{\mathrm{T}}=\begin{Bmatrix}\mathbf{q}&Q&\dot{\mathbf{q}}&\dot{Q}\end{Bmatrix}^{\mathrm{T}}, \tag{29a}$$

$$\{\dot{\boldsymbol{\chi}}\}=[\mathbf{A}]\{\boldsymbol{\chi}\}+[\mathbf{B}]\{\mathbf{u}\}+[\hat{\mathbf{B}}]\{\mathbf{u}_d\}. \tag{29b}$$

When Eq. (28) is presented in a standard state space form, Eq. (29b) is obtained where $[\mathbf{A}]$ is the state transition matrix, $\{\boldsymbol{\chi}\}$ is the state space variables vector, $\{\mathbf{u}\}$ is the control input vector (that contains the V voltage input) and $\{\mathbf{u}_d\}$ is the disturbance input vector. Also,

$$[\mathbf{A}]=\begin{bmatrix}\mathbf{0}&0&\mathbf{I}&0\\0&0&\mathbf{0}&1\\-\mathbf{M}^{-1}\mathbf{K}_{qq}&-\mathbf{M}^{-1}\mathbf{K}_{qQ}&-\mathbf{M}^{-1}\mathbf{C}&0\\-L^{-1}\mathbf{K}_{Qq}&\{K_{QQ}\}&\mathbf{0}&-L^{-1}R\end{bmatrix},\quad[\mathbf{B}]=\begin{bmatrix}\mathbf{0}\\0\\L^{-1}\\0\end{bmatrix},\quad[\hat{\mathbf{B}}]=\begin{bmatrix}\mathbf{0}\\0\\-[\mathbf{M}]^{-1}[\mathbf{F}]\\0\end{bmatrix}. \tag{30}$$

Here the nonlinear term $\{K_{QQ}\}$ is embedded in the state transition matrix $\mathbf{A}$ and is given by

$$\{K_{QQ}\}=-L^{-1}\left(\frac{h_{pz}}{A^e}(g_{31}h_{31}+g_{312}h_{32})+\frac{h_{pz}}{\boldsymbol{\chi}_3}\mathrm{IM}\left\{\beta_{33}^{\sigma}\frac{\boldsymbol{\chi}_3}{A^e}\right\}\right). \tag{31}$$

4. Experiment and simulation results

4.1. Experimental identification

Model identification for the Ishlinskii hysteresis operator is conducted using the same procedure used to identify the classical Preisach hysteresis model [5]. A monotonically increasing and then monotonically decreasing input is given to the system to form the first- and second-order reversal curves (Fig. 5). Using a set of first-order reversal curves, the Everett function $F(\alpha',\beta')$ is obtained which can be defined as

$$F(\alpha',\beta') = \frac{f_{\alpha'} - f_{\alpha'\beta'}}{2}. \tag{32}$$

The relationship between the classical Preisach and Ishlinskii model was defined in Eqs. (7), (9) and (10). The weighting function $\mu(\alpha',\beta')$ used in these equations can be defined as the second derivative of the Everett function:

$$\mu(\alpha',\beta') = -\frac{\partial^2 F(\alpha',\beta')}{\partial\alpha'\partial\beta'}. \tag{33}$$

For the identification of the elasto-slide elements, the Everett function is sufficient and double differentiation for evaluation of the weighting function is not necessary [29,30].

A PSI-5H4E type PZT actuator (Piezo Systems, Inc., Cambridge, MA, USA) is studied. Initially, the specimen is tested without being bonded to a plate with free–free boundary conditions approximated by resting the wafer at its center of gravity on a sponge cube ($0.5 \times 0.5 \times 0.5\,\mathrm{cm}^3$). For electrical excitation an amplifier (Model P0623A, Trek, Medina, NY, USA) is used that enables current and applied electric field monitoring. The response of the system is measured by using 2 laser Doppler vibrometers (LDV) (Polytec CLV 1000 and PDV100). Measurements are taken on opposite sides of the wafer from the middle of the edge; measurements are repeated for 31 and 32 directions, as shown in Fig. 6.

The PZT wafer is first tested for congruency and wiping-out conditions, which are necessary and sufficient to establish that a classical Preisach model is applicable. It is not possible to check these conditions experimentally. For *any* minor hysteresis loop, however, these conditions were satisfied for the range of values tested. In Fig. 7 one can observe the same experimental minor hysteresis loops that are formed by the same reversal values of the input with a different prior history.

Having verified these conditions, the symmetric hysteresis loop is observed where the absolute value of output for the input maximum extrema and minima are almost the same (an assumption used in the Ishlinskii model). Next, Everett functions for the 2, 5, and 10 elasto-sliding elements are generated from experimental data shown in Fig. 8.

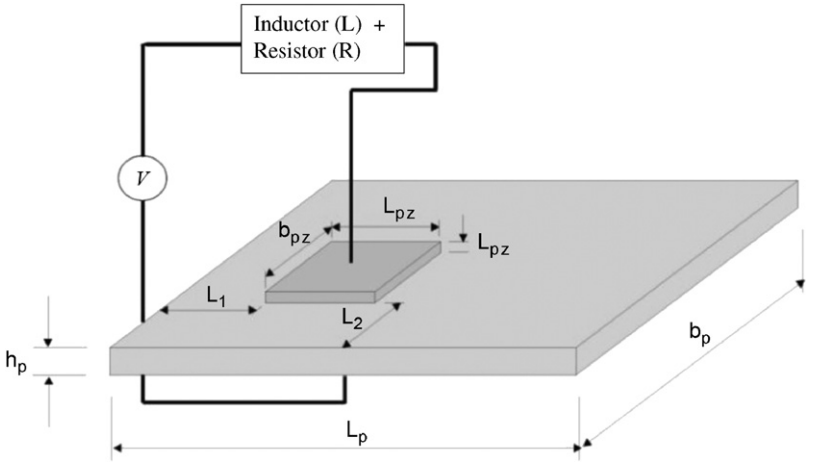

Fig. 5. Plate with a sensor and an actuator piezo layer for possible active, passive or hybrid control.

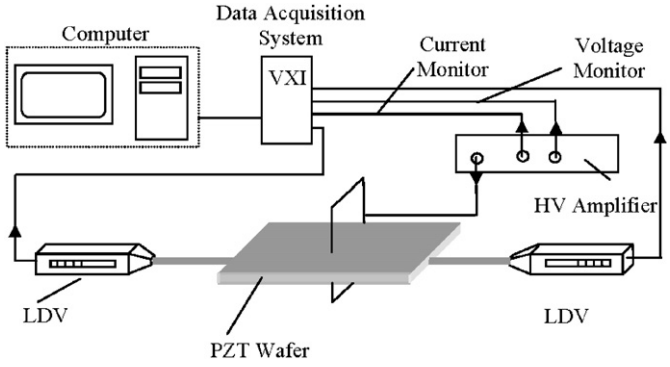

Fig. 6. Experimental setup.

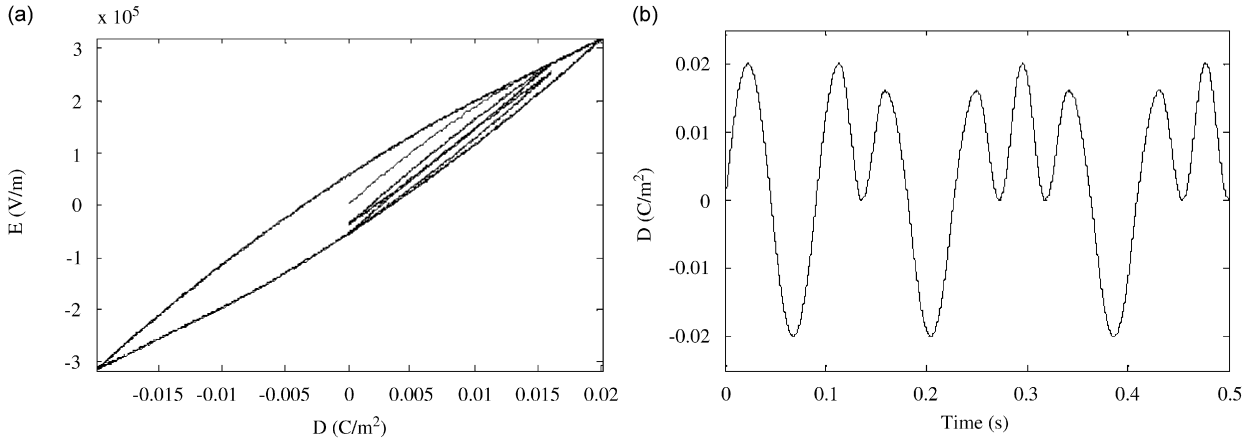

Fig. 7. (a) Experimental congruency loops and (b) electric displacement time plot for the congruency loops.

Utilizing the Everett functions, dielectric impermeability (β^{σ}) under uniform stress and the equivalent friction force e^{i}_{rc} constants for each block are identified. Accordingly, the constants for 3 different sets (2, 5 and 10 element sets) are used with Eq. (8) for simulating the experiment conducted at 10 Hz, where the PZT itself was excited without bonding it to a structure.

Experimentally identified Ishlinskii parameters are given in Table 1 where the first friction force equivalent e^{i}_{rc} constant is infinite to simulate the fixed spring effect that is necessary at saturation locations. The experimental and simulation results are shown in Fig. 9 where simulations are conducted with 2, 5 and 10 elements. It can be seen that as the element number is increased from 2 to 10, the accuracy of the model has increased for both electric displacement vs. electric field and electric field vs. mechanical strain. The hysteresis loop shape as well the area within it approach experimental values as n increases. Similarly, the simulated congruency loops are in agreement with the experiment (Fig. 10a and b). (Note, referring to Fig. 9a, the input D starts at zero, increases to a maximum value monolithically, and then begins decreasing in amplitude monolithically as it cycles from positive to negative values, and then back to positive, etc. Consequently, it is not expected that the initial line from the origin to the positive maxima will encompass all later trajectories in the D vs. E plane.)

4.2. Experimental and simulation results for PZT coupled to structure

The PZT actuator wafer is bonded to a simply supported plate similar to the one shown in Fig. 5. The mechanical and electrical coefficients of the system are given in Table 2. Bonding to the aluminum plate

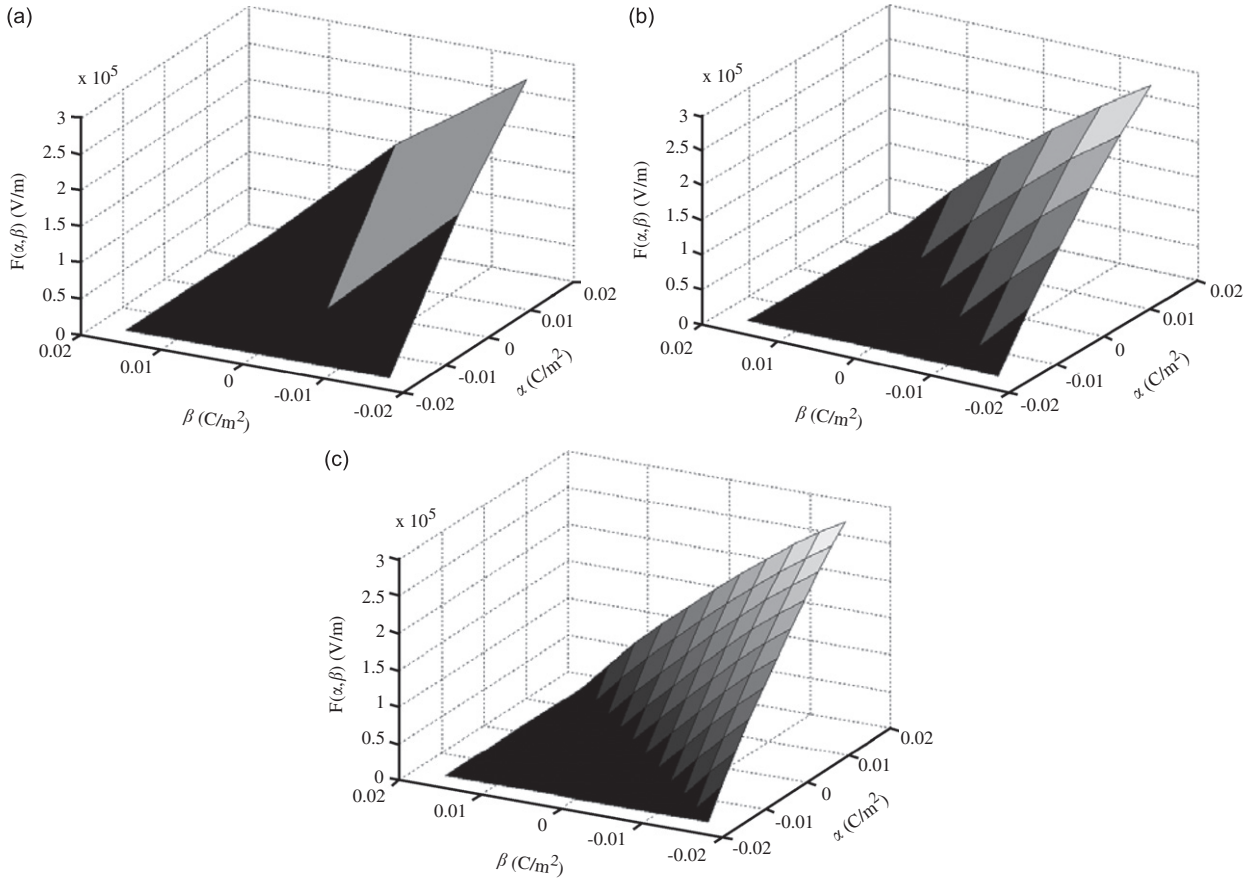

Fig. 8. Everett function surface plots: (a) 2 sliding elements; (b) 5 sliding elements and (c) 10 sliding elements.

Table 1
Ishlinskii model parameters for 2, 5 and 10 sliding elements

Number of elements, n	Equivalent friction forces, e^i_{rc}	Dielectric impermeability constant β^{σ_i}
2	$(\infty, 4.9821) \times 10^4$	$(1.4623, 0.5679) \times 10^7$
0	$(\infty, 3.9071, 1.8775, 1.3327, 1.1668) \times 10^4$	$(1.2873, 0.2783, 0.1783, 0.1899, 0.3325) \times 10^7$
10	$(\infty, 2.1038, 1.5327, 1.1341, 0.8679, 0.6924, 0.5698, 0.4663, 0.3523, 0.1978) \times 10^4$	$(1.1836, 0.1436, 0.1177, 0.0995, 0.0889, 0.0851, 0.0875, 0.0955, 0.1082, 0.1215) \times 10^7$

(base layer) and soldering of the wires was done by using Epo-Tek301 epoxy, #30 gage wires, S60 Sn/40Pb solder and Supersafe #67 DSA liquid flux. Simply supported plate conditions for the base layer are obtained by flexible brass shims that are mounted on each side of the plate. These shims are rigidly connected to a base so that they prevent transversal displacement of the plate yet allow rotation at the boundary.

The verification of the nonlinear multilayered model is done by using a 6×12 element meshing with quadratic serendipity elements where each element has 8 nodes with 5 degrees of freedom. The system is excited with a sine wave of 40 V amplitude using the PZT wafer. The transverse velocity response of the system is obtained via laser Doppler velocimeter measurements and integrated to yield displacement. The applied electric field and electric displacement values are recorded from the current and voltage monitor of the Trek (610D-G) amplifier. As this system is far more complicated than the wafer by itself, experimental and

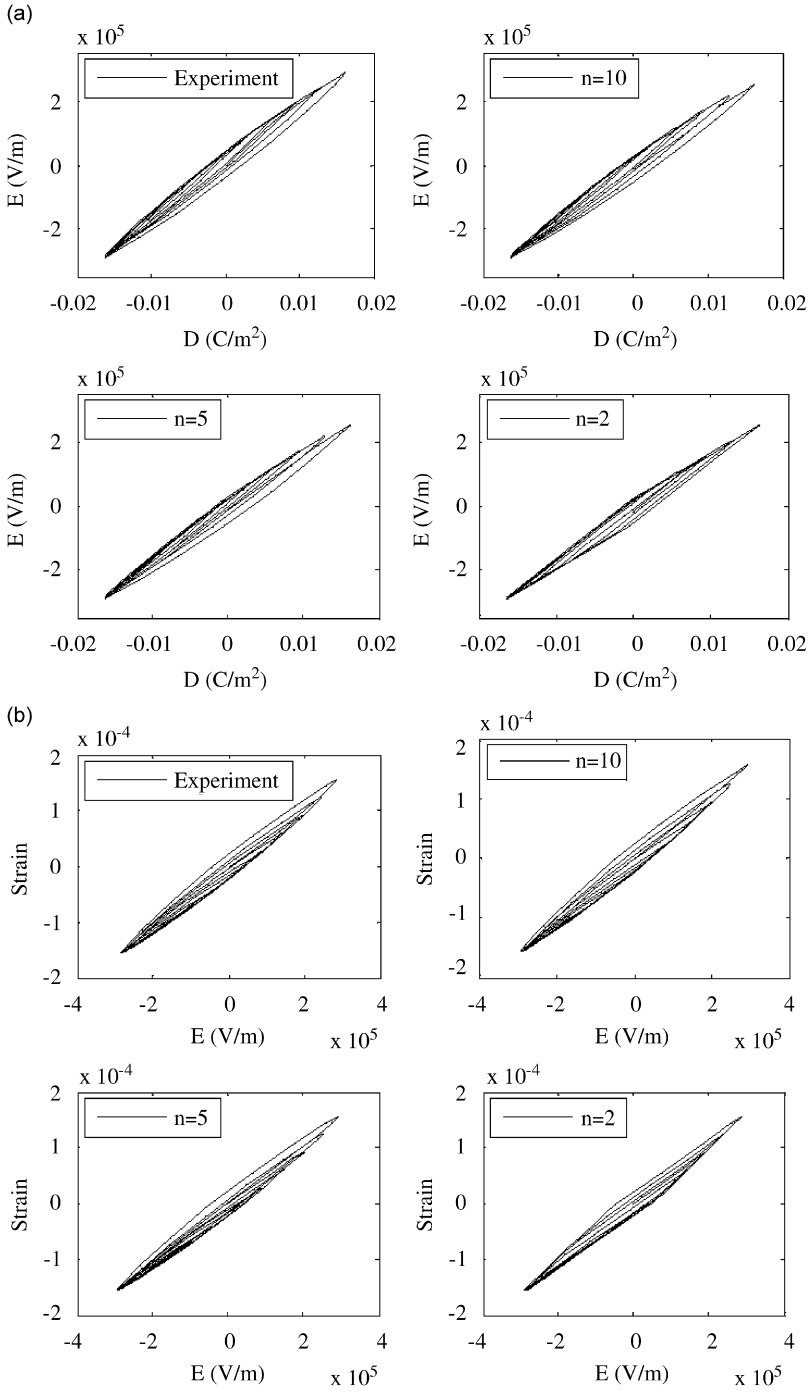

Fig. 9. Experimental and simulation results for free–free boundary conditions of the PZT by itself: (a) electric displacement vs. electric field and (b) electric field vs. mechanical strain.

simulation results that are presented are after the dominant transient behavior of the system has died out and the system is nearly in a steady-state condition. For this study at low frequencies, a 40 Hz low pass filter has been applied to the experimental data in order to filter out higher frequency noise.

In Fig. 11 experimental and simulated hysteresis loops for electric displacement vs. electric field as well as electric field vs. transverse displacement can be seen, where the nonlinear simulation and linear simulation

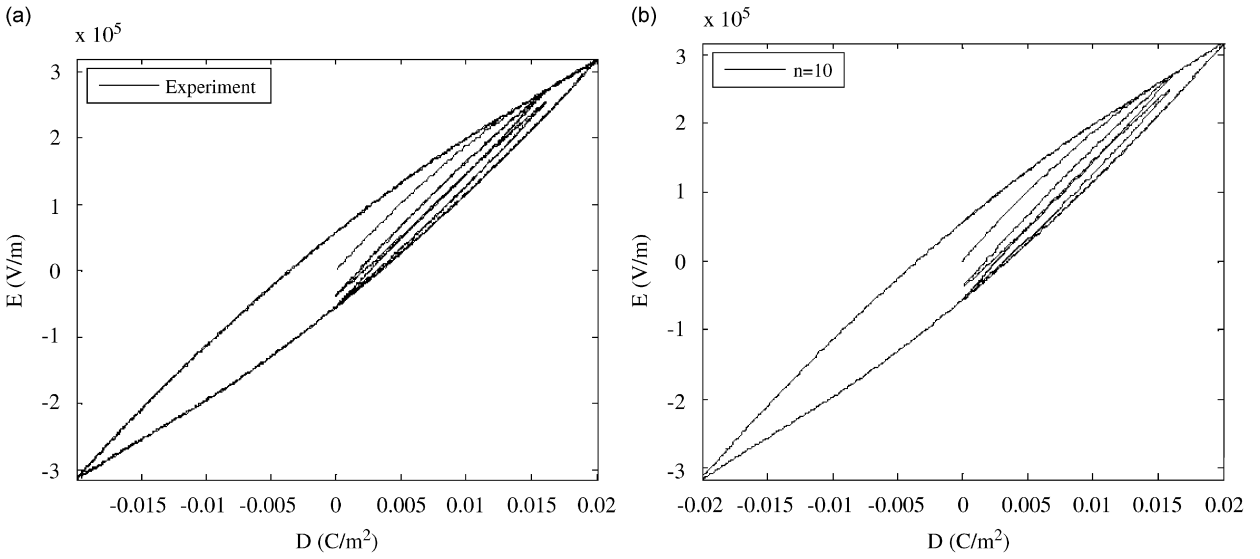

Fig. 10. (a) Experimental and (b) simulated congruency loops using 10 sliding elements for free–free boundary conditions of the PZT by itself.

Table 2
Mechanical and electromechanical properties and dimensions of the system used for control application

	Base layer	Piezo layer	Units
Length			
L_p, L_{pz}	0.6096	0.07239	m
Width			
b_p, b_{pz}	0.3048	0.07239	m
Thickness			
h_p, h_{pz}	0.003098	0.0002667	m
L_1	–	0.2686	m
L_2	–	0.1162	m
Density			
ρ	2713	7800	kg/m^3
Young modulus			
E	7.2×10^{10}	6.2×10^{10}	N/m^2
g_{31}	–	$(-9.5) \times 10^{-3}$	V m/N
h_{31}	–	$(-9.6429) \times 10^{8}$	V/m
Dielectric constant			
β_{33}^{T}	–	16,408,026	V m/C

results are shifted on the y-axis for visualization. The simulated hysteresis loops in both Figs. 11(a) and (b) are in good agreement with those from the experiment. In general, the experimental and simulation match for mechanical displacement is very challenging due to the mechanical damping, which needs to be carefully estimated. In the presented simulation, modal damping values are obtained via MEScope software and the damping matrix $\mathbf{C}$ in Eq. (28) is formulated. In Fig. 12 the nonlinear and linear simulation time domain responses of the transverse displacement and the electric displacement are shown along with the experimental results. It is observed that there is a slight phase shift between the experiment and the linear case results, while the phase of the nonlinear simulation results is close to that observed in the experiment. The main reason for the delay in the experiment and nonlinear simulation is the hysteresis phenomenon.

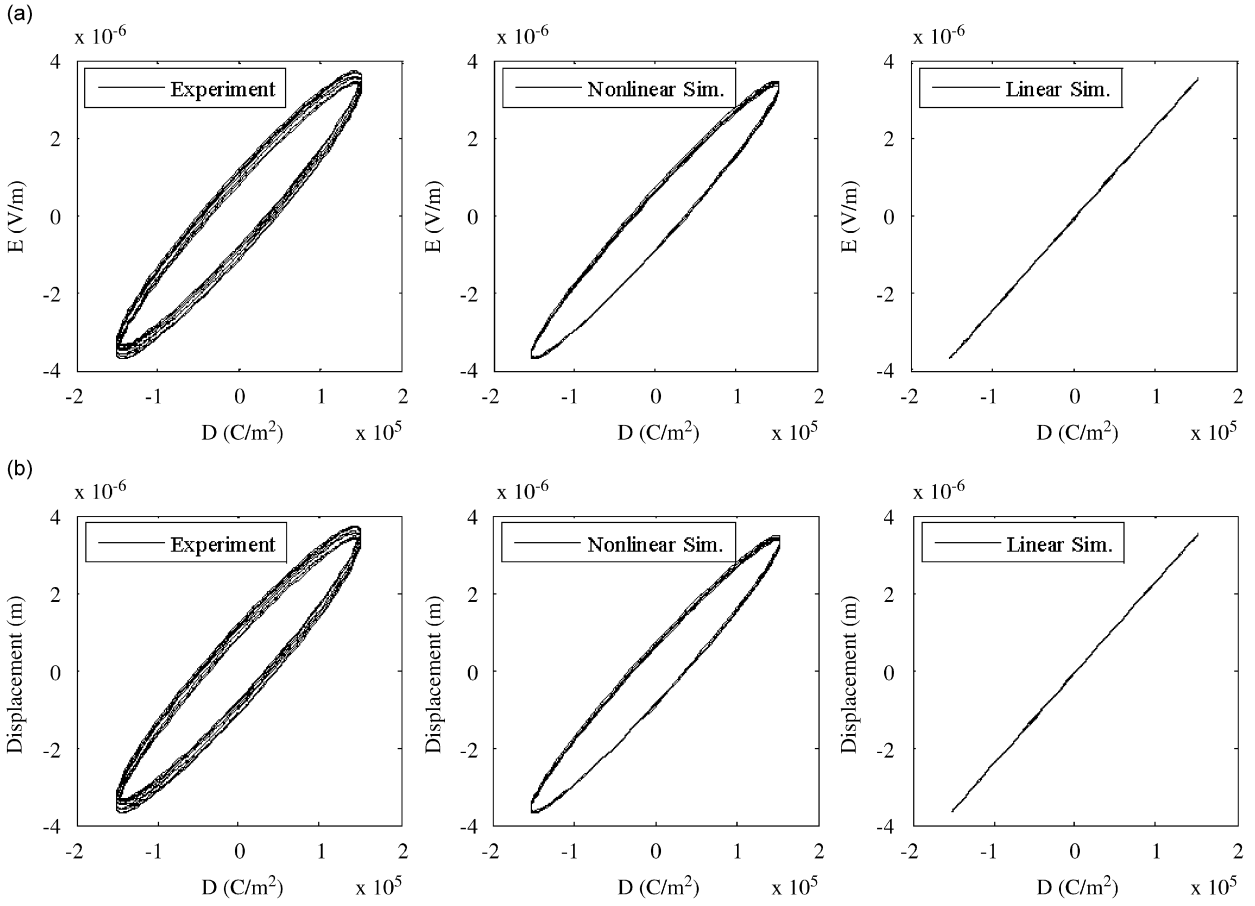

Fig. 11. Hysteresis loop plots for PZT + plate: (a) electric field vs. electric displacement and (b) electric field vs. transverse displacement.

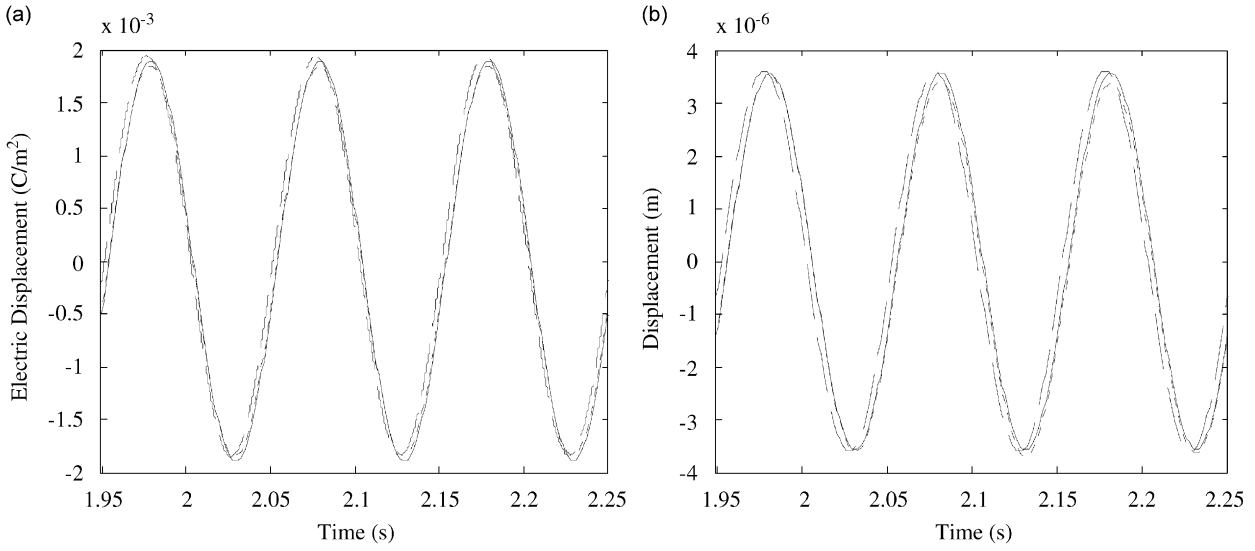

Fig. 12. Hysteresis loop plots for the PZT laminated on the plate: (a) electric field vs. electric displacement and (b) electric field vs. transversal displacement. ((……) experiment, (———) nonlinear simulation, (— — —) linear simulation).

Experimental validation of the method shows that for excitation frequency values that are close to the identification frequency, the model is accurate. However, as the identification and excitation frequencies become further apart the accuracy of the model decreases. When the excitation frequency is greater than the identification frequency, the hysteresis loop widens and the total hysteresis energy loss increases. This phenomenon is mainly due to some rate dependency of the hysteresis not captured by the Ishlinskii model and also due to the frequency dependence of the structural damping.

As the Ishlinskii hysteresis model is a rate-independent function, for simulation of multiple excitation frequencies that are not close to each other, the system parameters should be identified for each frequency band. One other possible way for taking the rate dependency into account is to introduce dependence on the rate of the input into the weighting function μ in Eq. (7), which would then be expressed as

$$f(t) = \iint_{\alpha \geqslant \beta} \mu\left(\alpha, \beta, \frac{\mathrm{d}u}{\mathrm{d}t}\right) \gamma_{\alpha\beta}[u(t)] \, \mathrm{d}\alpha \, \mathrm{d}\beta. \tag{34}$$

The mechanical equivalent of this new term in the function is a viscous damper. This rate-dependent enhancement to the hysteresis function is left for future studies, it has the potential to expand the introduced model's bandwidth of accuracy.

5. Conclusion

The hysteresis effect in piezoceramic structures is implemented in a finite element method that uses laminated Mindlin plate theory. The rate-independent Ishlinskii model, a type of classical Preisach model that has been shown to accurately simulate piezoceramic hysteresis, is adapted for the finite element method. A state space representation is introduced with nonlinear terms for transient and steady-state response simulation. Hysteresis operator parameter identification is briefly reviewed and the model is validated via experimental studies. The accuracy of the overall finite element model can be increased by increasing the number of the elasto-sliding elements in the hysteresis model, this was shown by comparing the simulation and experimental results. Some rate-dependence in the piezoceramic hysteresis was observed. Hence, to increase the bandwidth where the introduced model is accurate a rate-dependent parameter would be required in the hysteresis model; this is left for future studies.

References

[1] I.D. Mayergoyz, G. Friedman, Generalized Preisach model of hysteresis, *IEEE Transactions on Magnetics* 24 (1988) 212–217.
[2] I.D. Mayergoyz, Dynamic Preisach models of hysteresis, *IEEE Transactions on Magnetics* 24 (1988) 2925–2927.
[3] A.A. Adly, I.D. Mayergoyz, A. Bergqvist, Preisach modeling of magnetostrictive hysteresis, *Journal of Applied Physics* 69 (1991) 5777–5780.
[4] A.A. Adly, I.D. Mayergoyz, Experimental testing of the average Preisach model of hysteresis, *IEEE Transactions on Magnetics* 28 (1992) 2268–2270.
[5] I.D. Mayergoyz, *Mathematical Models of Hysteresis and their Applications*, Elsevier, Boston, 2003.
[6] F. Delince, A. Nicolet, F. Henrotte, A. Genon, W. Legros, Influence of hysteresis on the behavior of coupled finite element–Electric circuit models, *IEEE Transactions on Magnetics* 30 (1994) 3383–3386.
[7] F. Henrotte, A. Nicolet, F. Delince, A. Genon, P.W. Legros, Modeling of ferromagnetic materials in 2D finite element problems using Preisach's model, *IEEE Transactions on Magnetics* 28 (5) (1992) 2614–2616.
[8] P.J. Leonard, D. Rodger, T. Karagular, P.C. Coles, Finite element modelling of magnetic hysteresis, *IEEE Transactions on Magnetics* 31 (1995) 1801–1804.
[9] V. Basso, G. Bertotti, O. Bottauscio, F. Fiorillo, M. Pasquale, Power losses in magnetic laminations with hysteresis: finite element modeling and experimental validation, *Journal of Applied Physics* 81 (1997) 15.
[10] N. Takahashi, S. Miyabm, K. Fuji, Problems in practical finite element analysis using Preisach hysteresis model, *IEEE Transactions on Magnetics* 35 (1999) 1243–1246.
[11] P. Ge, M. Jouaneh, Modeling hysteresis in piezoceramic actuators, *Precision Engineering* 17 (1995) 211–221.
[12] B. Jung, W. Kim, Improvement of scanning accuracy of PZT piezoelectric actuators by feed-forward model reference control, *Precision Engineering* 16 (1994) 49–55.

[13] J. Coutte, P. J. Debus, B. Debus, R. Bossut, C. Granger, G. Haw, Finite element modeling of PMN electrostrictive materials and application to the design of transducers, *Proceedings of the Annual IEEE International Frequency Control Symposium,* Pasadena, CA, 1998, pp. 703–708.
[14] R. Simkovics, H. Landes, M. Kaltenbacher, R. Lerch, Nonlinear finite element analysis of piezoelectric transducers, *Proceedings of the IEEE Ultrasonics Symposium I*, Vol. 2, Caesars Tahoe, NV, 1999, pp. 1057–1060.
[15] R. Simkovics, H. Landes, M. Kaltenbacher, Finite element analysis of ferroelectric hysteresis effects in piezoelectric transducers, *Proceedings of the IEEE Ultrasonics Symposium,* Vol. 2, Puerto Rico, 2000, pp. 1081–1084.
[16] D. Song, C.J. Li, Modeling of piezo actuators nonlinear and frequency dependent dynamics, *Mechatronics* 9 (1999) 391–410.
[17] M. Goldfarb, N. Celanovic, Modeling Piezoelectric stack actuators for control of micromanipulation, *IEEE Control Systems Magazine* 17 (1997) 69–79.
[18] P. Krejci, K. Kuhnen, Inverse control of systems with hysteresis and creep, *IEEE Proceedings on Control Theory and Applications* 148 (2001) 185–192.
[19] M. Kamlah, U. Bohle, Finite element analysis of piezoceramic components taking into account ferroelectric hysteresis behavior, *International Journal of Solids and Structures* 38 (2001) 605–633.
[20] L. Chuntao, T. Yonghong, A neural networks model for hysteresis nonlinearity, *Sensors and Actuators A* 112 (2004) 49–54.
[21] J. Fuzi, Experimental verification of a dynamic hysteresis model, *Physica B* 343 (2004) 80–84.
[22] S.E. Zirka, Y.I. Moroz, P. Marketos, A.J. Moses, Dynamic hysteresis modeling, *Physica B* 343 (2004) 90–95.
[23] E. Cardelli, G. Finocchio, E. Pinzaglia, Increasing the accuracy of the numerical identification of the modified scalar Preisach model, *IEEE Transactions on Magnetics* 40 (2004) 892–895.
[24] Y. Pasco, A. Berry, A hybrid analytical/numerical model of piezoelectric stack actuators using a macroscopic nonlinear theory of ferroelectricity and a Preisach model of hysteresis, *Journal of Intelligent Material Systems and Structures* 15 (2004) 375–386.
[25] R.C. Smith, S. Seelecke, Z. Ounaies, A free energy model for piezoceramic materials, *Proceedings of the SPIE's 2002 North American Symposium on Smart Materials and Structures*, San Diego, CA, Vol. 4693, 2002, pp. 183–190.
[26] R. Smith, M. Dapino, S. Seelecke, Free energy model for hysteresis in magnetostrictive transducers, *Journal of Applied Physics* 93 (2003) 458–466.
[27] S.E. Zirka, Y.I. Moroz, P. Marketos, A.J. Moses, Congruency-based hysteresis models for transient simulation, *IEEE Transactions on Magnetics* 40 (2004) 390–399.
[28] T.J. Royston, B.H. Houston, Modeling and measurement of nonlinear dynamic behavior in piezoelectric ceramics with application to 1–3 composites, *Journal of the Acoustical Society of America* 104 (1998) 2814–2827.
[29] S.-H. Lee, T.J. Royston, G. Friedman, Modeling and compensation of hysteresis in piezoceramic transducers for vibration control, *Journal of Intelligent Material Systems and Structures* 11 (2000) 781–790.
[30] S.-H. Lee, M.B. Ozer, T.J. Royston, Piezoceramic hysteresis in the adaptive structural vibration control problem, *Journal of Intelligent Material Systems and Structures* 13 (2002) 117–124.
[31] M. Goldfarb, N. Celanovic, A lumped parameter electromechanical model for describing the nonlinear behavior of piezoelectric actuators, *ASME Journal of Dynamic Systems, Measurement and Control* 119 (1997) 478–485.
[32] S.-H. Lee, M.B. Ozer, T.J. Royston, Hysteresis models for piezoceramic transducers, *Journal of Materials Processing and Manufacturing Science* 9 (2000) 33–52.
[33] Z.K. Kusculuoglu, T.J. Royston, Finite element formulation of composite plates with piezoceramic layers for optimal vibration control applications, *Smart Materials and Structures* 14 (2005) 1139–1153.